CrossMark
← click for updates

Deprotonated guanine·cytosine and 9-methylguanine·cytosine base pairs and their "non-statistical" kinetics: a combined guided-ion beam and computational study†

Wenchao Lu[ab] and Jianbo Liu*[ab]

We report a guided-ion beam mass spectrometric study on collision-induced dissociation (CID) of deprotonated guanine(G)·cytosine(C) base pairs and their 9-methylguanine (9MG) analogue with Xe, including measurements of product cross sections as a function of collision energy and determination of dissociation thresholds. DFT, RI-MP2 and DLPNO-CCSD(T) calculations and Rice–Ramsperger–Kassel–Marcus (RRKM) modeling were performed to elucidate structures and kinetics. The experiment and theoretical study have provided considerable insight into tautomerization, intra-base-pair proton transfer and dissociation of deprotonated G·C and 9MG·C. In contrast to the previously reported lowest-energy deprotonated base pair structure G·[C−H1]⁻ that consists of H-bonded neutral guanine and N1-deprotonated cytosine, we found that proton transfer from guanine N1 to cytosine N3 within G·[C−H1]⁻ (or 9MG·[C−H1]⁻) leads to another slightly more stable conformer denoted as G·[C−H1]⁻_PT1 (or 9MG·[C−H1]⁻_PT1). The conventional (non-proton-transferred) and the proton-transferred conformers are close in energy and interconvert quickly, but they can be distinguished by dissociation products. The conventional structure dissociates into deprotonated cytosine and neutral guanine, while the other dissociates into deprotonated guanine and neutral cytosine. The two dissociation asymptotes have similar threshold energies, but surprisingly the CID product mass spectra of deprotonated G·C and 9MG·C are both overwhelmingly dominated by deprotonated G or 9MG, with their branching ratios greater than RRKM predictions by one to two orders of magnitude. The proton-transferred structures of deprotonated base pairs and the "unexpected" non-statistical kinetics provide new leads for understanding purine–pyrimidine interactions, forming rare nucleobase tautomers, and base pair opening.

1 Introduction

When ionizing radiation interacts with living organisms, the energy deposited in cells produces abundant low-energy electrons which can be captured by DNA.[1] This process is initiated by dissociative electron attachment, and the rapid decay of the formation of transient anions may lead to deprotonation of nucleobases within DNA.[2] Alternatively, nucleobases may be deprotonated by acid–base equilibria with the surrounding environment. Deprotonation of nucleobases induces genotoxic damage by mispairing of complementary bases and consequent

genetic mutations, and plays a crucial rule in DNA oxidation, enzymatic reactions, *etc.*[3] For example, guanine is the most easily oxidized nucleobase of the four DNA nucleobases,[4–8] and is the major DNA target in ¹O₂-mediated photodynamic therapy.[9] We found that deprotonated guanosine exhibits a distinctively different ¹O₂ oxidation mechanism and reaction intermediate compared to its neutral and protonated analogues.[10] This may lead to synergetic effects of ionization and oxidation on guanine-containing oligonucleotides and DNA, which will be of practical interest in combining radiotherapy and photodynamic therapy for cancer.

One issue in the investigation of nucleobase deprotonation in DNA concerns proton transfer within purine–pyrimidine base pairs.[11–21] Intra-base-pair proton transfer is unfavorable for neutral complexes;[12,13] but could be promoted by a positive hole[11,14,15,17–21] or an excess electron[16,21,22] localized on a nucleobase moiety. Considering the latter possibility, identification of actual deprotonation sites in deprotonated base pairs and determination of accompanying structural perturbations and

a Department of Chemistry and Biochemistry, Queens College of the City University of New York, 65-30 Kissena Blvd., Queens, NY 11367, USA. E-mail: jianbo.liu@qc.cuny.edu; Tel: +1-718-997-3271

b Ph.D. Program in Chemistry, The Graduate Center of the City University of New York, 365 5th Ave., New York, NY 10016, USA

† Electronic supplementary information (ESI) available: Structures and Cartesian coordinates of all tautomers/rotamers of [G−H]⁻, 9MG, [9MG−H]⁻, C, [C−H]⁻, [G·C−H]⁻, [9MG·C−H]⁻, and TSs in Fig. 6. See DOI: 10.1039/c6cp06670d

energetic changes become essential for elucidating the underlying cause and mechanism of ionization-induced biological sequelae. The resulting information is also useful for developing DNA-templated nanowires and tailoring charge transfer dynamics along the DNA double helix.[23]

Herein, we report a combined experimental and computational study on deprotonated guanine·cytosine $[G·C–H]^-$ and 9-methylguanine·cytosine $[9MG·C–H]^-$ base pairs, the latter of which introduces a methyl group into the guanine moiety to mimic the presence of the sugar-phosphate backbone and block N9H–N7H tautomerization. Theoretical investigation of protonated/deprotonated G·C pairs has outpaced experiments.[18,19,24] Schaefer and his co-workers identified ten different structures for $[G·C–H]^-$ at the B3LYP/DZP++ level.[24] The most favorable structure was claimed to retain the conventional Watson–Crick (WC) H-bonding motif with a proton being abstracted from the N1 site of the cytosine moiety.[24] Structures with a proton removed from the guanine moiety were calculated to lie in an energy of at least 0.5 eV higher. However, no experiment was pursued to explore these structures.

In the present work, we have investigated collision-induced dissociation (CID) of $[G·C–H]^-$ and $[9MG·C–H]^-$ using guided-ion beam tandem mass spectrometry. CID was done by colliding base pair anions with Xe, eliminating complications from chemistry of the target. Dissociation thresholds were extracted from the collision energy (E_{col}) dependence of the CID cross section in the near threshold energy range.[25] An interesting finding is that the CID products of $[G·C–H]^-$ and $[9MG·C–H]^-$ are dominated by deprotonated G or 9MG rather than deprotonated C, over the entire E_{col} range of 0.1–5.0 eV. The anomalous dissociation indicates a deprotonated base pair structure that is different from those proposed by Schaefer's group.[24] We will show in the following that the most likely structures of $[G·C–H]^-$ and $[9MG·C–H]^-$ correspond to an intra-base-pair proton-transferred conformation. Guided-ion beam measurements, along with rigorous electronic structure calculations and statistical modeling at the density functional theory (DFT), RI-MP2 and CCSD(T) levels of theory, have provided unprecedented insight into the formation, interconversion and dissociation of deprotonated base pairs. The anomalous dissociation kinetics present in this work has important biological implications considering that base pair opening is required in many fundamental processes in cells, such as sequence recognition by proteins, DNA replication and transcription.[26,27]

2 Experimental and computational methods

2.1 CID of deprotonated base pairs

A home-built guided-ion beam tandem mass spectrometer was used to investigate CID product ions of deprotonated base pairs. The details of this apparatus have been described previously,[28] along with the operation, calibration and data analysis procedures. A brief description is given here, emphasizing the most relevant conditions of this experiment. The apparatus consists of an electrospray ionization (ESI) source, a radio frequency (rf) hexapole ion guide, a quadrupole mass filter, an rf octopole ion guide surrounded by a scattering cell, a second quadrupole mass filter, and a pulse-counting electron multiplier detector. Both the quadrupole mass filters use Extrel 9.5 mm diameter tri-filter rods operating at 2.1 MHz (using Extrel 150 QC RF/DC power supplies) to cover a mass/charge (m/z) range of 1–500.

A sample solution for generating $[G·C–H]^-$ or $[9MG·C–H]^-$ was prepared in HPLC grade ethanol/water (3 : 1 vol. ratio) containing 0.5 mM guanine (98%, Aldrich) or 9MG ($\geq$98%, Aldrich), 1.0 mM cytosine ($\geq$98%, Alfa Aesar) and 0.5 mM NaOH. The solution was sprayed into the ambient atmosphere through an electrospray needle, using a syringe pump at a flow rate of 0.06 mL h^{-1}. The ESI needle was held at -2.25 kV relative to ground for producing negatively charged species. Charged droplets entered the source chamber of the mass spectrometer through a pressure-reducing desolvation capillary, which was held at -110 V and heated to 140–150 °C. The distance between the tip of the ESI needle and the sampling orifice of the capillary was 5 mm. Charged droplets underwent desolvation as they passed through the heated capillary, and were converted into gas–phase complexes in the source chamber.

A skimmer with an orifice of 0.99 mm is located 3 mm from the capillary end, separating the source chamber and the hexapole ion guide. The skimmer was biased at -15 to -20 V relative to ground. The electrical field imposed between the capillary and the skimmer removed residual solvent molecules by collision-induced desolvation, and prevented large clusters from depositing downstream. Ions that emerged from the skimmer were transported into the hexapole at a pressure of 22 mTorr, undergoing collisional focusing and cooled to $\sim$310 K. Ions subsequently passed into a conventional quadrupole for the selection of specific base pair ions. Mass-selected base pair ions were collected and injected into the octopole ion guide, which trapped ions in the radial direction, minimizing the loss of the reactant and product ions resulting from scattering. The octopole was operated at 2.6 MHz with a peak-to-peak rf amplitude of 600 V. The octopole was surrounded by the scattering cell containing the Xe gas (Spectral Gases, 99.995%). The cell pressure was controlled using a leak valve and measured using a capacitance manometer (MKS Baratron 690 head and 670 signal conditioner). After passing through the scattering cell, remaining base pair ions and fragment ions drifted to the end of the octopole, and then were mass analyzed by the second quadrupole, and counted by the electron multiplier.

The initial kinetic energy distributions of the $[G·C–H]^-$ and $[9MG·C–H]^-$ ion beams were determined by a retarding potential analysis (RPA)[29] that measures the intensity of the ion beam while scanning the DC bias voltage applied to the octopole. The measured initial kinetic energy of these ion beams was 0.96 eV, and their energy spreads were 0.9 eV. The DC bias voltage also allowed control of the kinetic energy of reactant ions in the laboratory frame (E_{Lab}). E_{Lab} can be converted into E_{col} in the center-of-mass frame using $E_{col} = E_{Lab} \times m_{neutral}/(m_{ion} + m_{neutral})$, where $m_{neutral}$ and m_{ion} are the masses of neutral Xe and base pair ions, respectively. Ion beam intensities were 7.5×10^4 counts per s

for [G·C–H]$^-$ and 1.1×10^5 counts per s for [9MG·C–H]$^-$, and constant within 10%. CID cross sections were calculated from the ratios of reactant and product ion intensities at each E_{col} (under single ion-molecule collision conditions), the pressure of Xe in the scattering cell, and the effective length of target gas cloud. To maintain multiple collision effects at an insignificant level, the pressure of Xe in the scattering cell was maintained in the range of 0.01–0.02 mTorr. In this range of pressures, the probability of a single collision between the base pair ion and Xe is 1.8–3.6%, and that of double collisions is < 0.1%. The majority of base pair ions (> 96%) passed through the cell without interacting with Xe at all.

To minimize variations in experimental conditions that might be caused by drifting potentials, changes in ion beam intensities, *etc.*, we cycled through different E_{col} values several times in the experiment. RPA was performed before and after each cycle to check the initial kinetic energy of the reactant ion beam. The entire experiment was repeated five times. Based on the reproducibility of measurements, the relative error of CID cross sections (*e.g.* uncertainty in comparing data for different E_{col} values) was estimated to be ~10%.

2.2 Electronic structure calculations and statistical modeling

Geometries of neutral and deprotonated G, 9MG and C monomers, deprotonated G·C and 9MG·C base pairs, and transition states (TSs) for inter-conversions of base pairs were optimized at the B3LYP/6-311++G(d,p) level of theory using Gaussian 09 (rev. D01),[30] and then screened by their relative stabilities. The B3LYP hybrid GGA functional has been proven to be efficient and reliable for describing G·C structures.[16–19,24,31] The basis set superposition error (BSSE) was taken into account in base pair calculations using counterpoise correction, except for TSs. A maximum BSSE of 0.05 eV was found in B3LYP/6-311++G(d,p) energies. The stability order of the complexes was not changed by including BSSE corrections. All TSs were verified as first-order saddle points, and the vibrational mode with an imaginary frequency corresponds to the associated reaction pathway. Aside from the local criterion, intrinsic reaction coordinate (IRC) calculations were carried out to identify reactant/product minima connected through the identified TSs. To explore the solvation effects on the conformational landscape, we have employed the polarized continuum model (PCM),[32] which creates solute cavities *via* a set of overlapping spheres in the DFT calculations of base pairs.

The electronic energies of the B3LYP/6-311++G(d,p) optimized structures were refined at a wide spectrum of higher levels of theory augmented by larger basis sets, including B3LYP/aug-cc-pVQZ, M06-2X/def2-QZVPPD, PWPB95/aug-cc-pVQZ, RI-MP2/aug-cc-pVTZ, and DLPNO-CCSD(T)/aug-cc-pVTZ. Of these methods, M06-2X is a hybrid meta-GGA functional expected to have excellent performance in describing H-bond interactions and proton transfer barriers.[21,33] PWPB95 is one of the recently developed double-hybrid-meta-GGA density functionals.[34] It is the least basis set dependent and in general more accurate and robust than other double hybrids. To prevent any skepticism that could arise from the DFT calculations, we also exploited the resolution

of the identity Møller-Plesset procedure (RI-MP2) which provides an accurate description of H-bonds.[35,36] We have verified that the RI-MP2 reaction PES for [G·C–H]$^-$ is almost identical to that obtained at the exact MP2 level, but the RI-MP2 method is much more efficient. Finally, the domain based local pair-natural orbital coupled-cluster method with single-, double- and perturbative triple excitations DLPNO-CCSD(T) was used to further assess and improve the accuracy of energy analysis for base-pair interactions.[37] All single point calculations were accomplished using ORCA 3.0.3.[38] The total energy reported at each level of theory is the summation of the electronic energy calculated at the specified level, and the 298 K thermal correction calculated at B3LYP/6-311++G(d,p). B3LYP/6-311++G(d,p) calculated vibrational frequencies and zero-point energies (ZPEs) were scaled by a factor of 0.952 and 0.988,[39] respectively. In PWPB95 calculations, RI-JK approximation for Coulomb and Exchange terms was used to accelerate calculations[38] and no difference was found in relative energies compared to those obtained using original PWPB95. No difference was observed with D3-BJ dispersion correction (using PWPB95-D3),[40,41] either.

Gas phase acidity (GPA) was calculated as GPA $= \Delta G_g^{\circ}([A-H]^-) + \Delta G_g^{\circ}(H^+) - \Delta G_g^{\circ}(A)$, where $\Delta G_g^{\circ}(A)$, $\Delta G_g^{\circ}([A-H]^-)$ and $\Delta G_g^{\circ}(H^+)$ stand for the standard Gibbs free energy for the neutral nucleobase, deprotonated nucleobase and proton, respectively. The dissociation threshold (E_0) of the deprotonated base pair was calculated as the energy difference between the base pair and the dissociated products that consist of a deprotonated base and its complementary base in the neutral state.

Rice–Ramsperger–Kassel–Marcus (RRKM)[42] rate constants were calculated with the program of Zhu and Hase,[43] using direct state count algorithm and scaled B3LYP/6-311++G(d,p) frequencies and B3LYP/aug-cc-pVQZ//B3LYP/6-311++G(d,p) energies. The angular momentum quantum number J for the reaction was determined from reactant rotational energy, assuming that the base pair can be roughly treated as a nearly symmetric top molecule since each base pair has two principle moments of inertia which are not very different. Product branching was determined by the ratio of RRKM rates for different channels.

3 Results and discussion

3.1 Structures and energies of [G·C–H]$^-$ and [9MG·C–H]$^-$

Separated nucleobases. Stable tautomers/rotamers of gas-phase neutral and deprotonated guanine and 9-methylguanine have been reported in our recent work.[8,10] In the present study, a total of fourteen tautomers/rotamers were identified for gas-phase neutral cytosine and nine for gas-phase deprotonated cytosine. For the sake of brevity, only the first four lowest-lying tautomers/rotamers of each series are presented in Fig. 1, along with their relative energies and populations at 298 K. A complete list of gas-phase neutral and deprotonated nucleobases can be found in Fig. S1–S5 (ESI†). Cytosine has keto–enol, amino–imino and N1H–N3H tautomerization.[44] The canonical tautomer C_1 (*i.e.* 1H-keto–amino) represents 79% of the thermal population in the gas phase. C_1 also dominates in
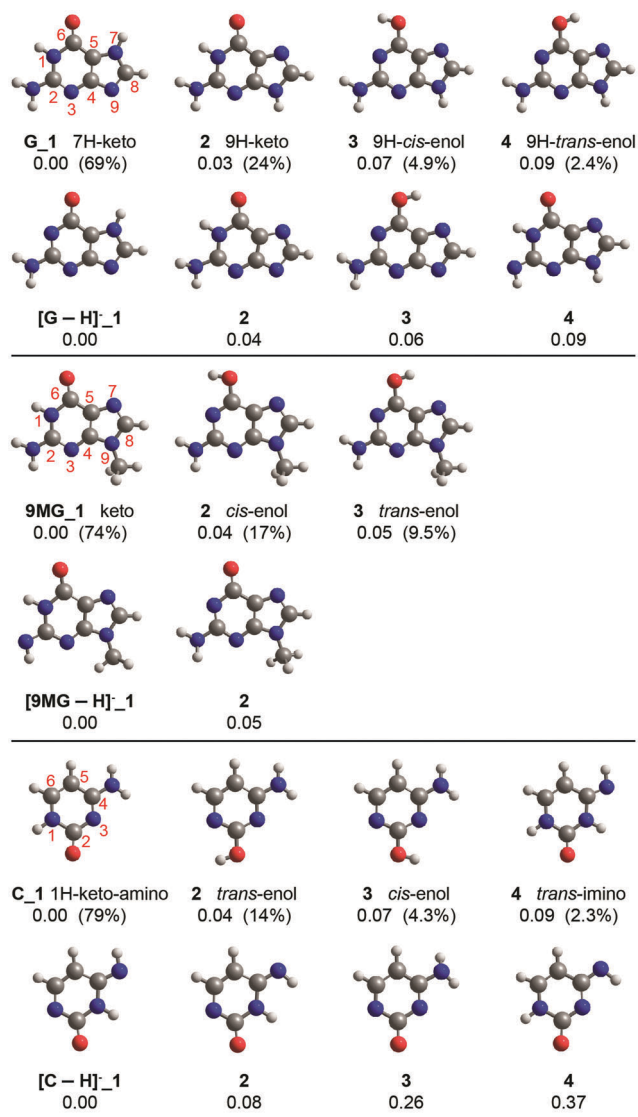
Fig. 1 Low-lying tautomers/rotamers of G, [G−H]⁻, 9MG, [9MG−H]⁻, C and [C−H]⁻. The numbering schemes and nomenclatures are presented. Relative energies (eV, with respect to global minima) and thermal populations (presented in parentheses) were evaluated based on the sum of electronic energies calculated at the B3LYP/aug-cc-pVQZ//B3LYP/6-311++G(d,p) level with thermal correction (298 K) at B3LYP/6-311++G(d,p).

aqueous solution according to the study by Trygubenko *et al.*[45] The remaining population is shared mostly by two enols C_2 (14%) and C_3 (4.3%). The keto and enol structures were found to co-exist with comparable abundances in gas-phase REMPI and IR-UV double-resonance spectra.[46,47] Note that Trygubenko *et al.* reported an RI-MP2-optimized enol as the global minimum for gas-phase cytosine, and keto is less stable by 0.05–0.11 eV and therefore accounts for only a few percentages of the population. This contrasts with DFT calculations in the literature[44] and in the present work, and with gas-phase spectroscopy,[46,47] all of which have shown that keto and enol are comparably important and keto is preferred at the DFT theory. The next stable tautomer is *trans*-imino C_4, which was predicted to lie 0.09 eV higher in energy than C_1 and accounts for only 2.3% of the population.

Albeit being minor, C_4 was detected by molecular beam microwaves, accompanying C_1 and 2.[48]

Cytosine may deprotonate at N1–H (or N3–H), the amino or the enol group. Theoretically, the two lowest-energy deprotonated structures are [C−H]⁻_1 and 2, which are formed upon deprotonation of N1–H in neutral imino tautomers C_4 and 5, respectively. However, neither of the two neutral iminos is significant. Considering that the deprotonated conformers in the electrospray were formed mostly by deprotonation of the dominant C_1 in solution,[45] [C−H]⁻_3 and 4 become the most likely structures, of which [C−H]⁻_3 was detected in gas-phase photoelectron spectra.[49]

In Table 1, we compared the B3LYP/aug-cc-pVQZ//B3LYP/6-311++G(d,p) calculated site-specific GPA values of the lowest-lying tautomers of guanine (including 7H-keto and 9H-keto tautomers, abbreviated by 7HG and 9HG henceforth), 9MG and cytosine. Theoretical and experimental GPA and pK_a values available in the literature are also gathered in the table. Our GPA calculations fall within the range of the reported values, and the best agreement was found in the case of 9HG.

[G·C–H]⁻. The starting geometries of gas-phase [G·C–H]⁻ were generated by removing a proton from the WC structure of neutral G·C. We have considered both 7HG and 9HG in the neutral base pair since both tautomers have significant populations in the gas phase and in solution.[57] For the cytosine moiety, only the 1H-keto–amino structure was adopted as this is the one that largely dominates in the gas phase and in solution as discussed above. The H1, H2a, H2b and H7 (or H9) of guanine and the H1, H4a and H4b of cytosine were considered as deprotonation sites in conformation search for [G·C–H]⁻, because the adjacent N atoms of these protons are most likely to hold an excess electron. The G·C pair has proton donor and acceptor properties, therefore the protons participating in the WC H-bonds were allowed to shuttle between the two subunits of [G·C–H]⁻, following three possible pathways denoted as PT1, PT2 and PT4 in the ChemDraw structure in Fig. 2, respectively. All three pathways were found to be feasible in protonated [G·C + H]⁺.[19,21,60] For [G·C–H]⁻, proton transfer should proceed in such a way that the neural monomer plays the role of a proton donor and the deprotonated one the role of a proton acceptor. The initial structures thus generated converged to a total of sixteen conformers as summarized in Fig. 2. A generic label is used to represent optimized structures, *e.g.* 7HG·[C–H]⁻_PT1 represents that a deprotonated base pair made up of a neutral 7HG and a deprotonated cytosine (with a proton abstracted from cytosine N1–H), and the suffix PT1 designates intra-base-pair proton transfer from guanine N1 to cytosine N3 *via* the PT1 pathway.

Note that the pK_a of guanine N7–H/N9–H is close to that of cytosine N1–H, but the gas-phase GPA of guanine N7–H/N9–H is much lower than that of cytosine N1–H (see Table 1). On the basis of the GPA values of individual nucleobases, one would anticipate that the proton may be abstracted from the guanine moiety, yielding [G−H]⁻·C as the lowest energy structure. In contrast to such an expectation, however, the most favorable deprotonated structures actually originate from the deprotonation of cytosine N1–H (*i.e.* G·[C–H1]⁻), indicating the large influence

This journal is © the Owner Societies 2016

Phys. Chem. Chem. Phys., 2016, **18**, 32222–32237 | **32225**

Table 1　Site-specific GPA and pK_a of the lowest-lying tautomers of guanine, 9MG and cytosine

Nucleobase	Site	Calc. GPA (kJ mol⁻¹)		Exp. GPA (kJ mol⁻¹)	pK_a
		This work[a]	Literature		
7HG	N1–H	1384	1369.0,[b] 1413.4/1407.5[c]	—	9.19*[j] 9.2–9.6[j]
	N7–H	1388	1369.4,[b] 1417.5/1414[c]	—	11.94*[j] 12.3–12.4[j]
9HG	N1–H	1393	1415.8,[d] 1423.0/1416.7,[c] 1397,[e] 1367.3[b]	1398 ± 17,[e] 1372 ± 13[b]	9.65*[j] 9.2–9.6[j]
	N9–H	1385	1407.4,[d] 1414.6/1411.7,[c] 1389,[e] 1368,[i] 1377.4[b]	1385 ± 17,[e] 1368 ± 8[i]	12.3–12.4[j]
9MG	N1–H	1392	—	—	9.56[k]
Cytosine	N1–H	1458	1444.2,[f] 1452.3/1446,[g] 1423,[e] 1410,[i] 1406[h]	1423 ± 8,[e] 1401 ± 8,[i] 1402 ± 13[h]	12.2[l]
	N4–H4b	1468	1457.9,[f] 1452,[e] 1461.9/1459,[g] 1423,[i] 1417.5[h]	1448 ± 8,[e] 1443 ± 17,[h] 1439 ± 15[i]	—
	N4–H4a	1489	1481.4,[f] 1482/1479,[g] 1477,[e] 1439,[i] 1441.8[h]	1448 ± 8,[e] 1439 ± 8[i]	—

[a] B3LYP/aug-cc-pVQZ//B3LYP/6-311++G(d,p) values. [b] Ref. 50, theoretical GPA at B3LYP/6-31+G* and experimental GPA using the Cooks kinetic method. [c] Ref. 51, GPA at B3LYP/aug-cc-pVTZ//B3LYP/6-31+G(d), derived from direct calculation/isodesmic reaction, respectively. [d] Ref. 52, presented as a deprotonation enthalpy at B3LYP/6-31++G(d,p). [e] Ref. 53, theoretical GPA was calculated using CURES-EC. [f] Ref. 54, presented as a deprotonation enthalpy at B3LYP/6-31++G(d,p). [g] Ref. 55, GPA at B3LYP/aug-cc-pVTZ//B3LYP/6-31+G(d), derived from direct calculation/isodesmic reaction, respectively. [h] Ref. 44, theoretical GPA at B3LYP/6-31+G* and experimental GPA using the bracketing method. [i] Ref. 56, theoretical GPA at CURSE-EC. [j] Ref. 57, calculated data are marked with asterisks. [k] Ref. 58. [l] Ref. 59.

of base pairing on ionization of nucleobases. Of the four lowest-lying G·[C–H1]⁻ conformers in Fig. 2, the first and the fourth are formed by pairing 7HG and [C–H1]⁻, and the second and the third are by 9HG and [C–H1]⁻. In each of the two combinations, one conformer has a conventional structure and the other has a proton-transferred structure, and the proton-transferred conformer is more stable than its conventional counterpart. This may be attributed to the lower acidity of guanine N1 and the higher proton affinity of cytosine N3.[19] The proton-transferred structures 7HG·[C–H1]⁻_PT1 and 9HG·[C–H1]⁻_PT1 have a shortened H4a···G(O6) bond and meanwhile a much elongated H2a···C(O2). Based on NBO charge analysis, the negative charge used to reside on the [C–H1]⁻ moiety in conventional structures redistributes to the guanine moiety after proton transfer, i.e. δ(7HG) = −0.13 in 7HG·[C–H1]⁻ vs. −0.87 in 7HG·[C–H1]⁻_PT1, and δ(9HG) = −0.03 in 9HG·[C–H1]⁻ vs. −1.00 in 9HG·[C–H1]⁻_PT1.

Deprotonation of guanine H1, H7 (or H9 in 9HG) and cytosine H4b makes the second tier low-energy conformers (within 0.65 eV energy range), including [7HG–H1]⁻·C, [9HG–H1]⁻·C, and [7HG–H7]⁻·C and their proton-transferred analogues [7HG–H7]⁻·C_PT4, 7HG·[C–H4b]⁻ and 7HG·[C–H4b]⁻_PT1, and 9HG·[C–H4b]⁻ and 9HG·[C–H4b]⁻_PT1. Removal of guanine H1 eliminates the middle H-bond; consequently the two bases slide and twist relative to each other so that they may form two new N···H–N bonds.[24] Removal of guanine H7 or cytosine H4b, on the other hand, maintains the WC motif, but twists the original planar structure (see Table 4). Compared to conventional [7HG–H7]⁻·C, 7HG·[C–H4b]⁻ and 9HG·[C–H4b]⁻ structures, their proton-transferred conformers are evaluated in energy—a trend that is different from that was found for the first tier low energy structures.

We attempted to locate a structure originating from deprotonating guanine H2a of G·C, but the starting structure collapsed in geometry optimization. Removal of cytosine H4a breaks the top H-bond. The resulting structures 7HG·[C–H4a]⁻ and 9HG·[C–H4a]⁻ feature considerable propeller twist angles (see Table 4)

and high energies. Similarly, the loss of guanine H2b breaks the bottom H-bond, leading to the two least stable conformers [9HG–H2b]⁻·C and [7HG–H2b]⁻·C.

Interesting findings are summarized for [G·C–H]⁻. First, it is the base pairing energy rather than individual nucleobase GPAs that determines the deprotonation site of the complex. Secondly, both PT1 and PT4 proton transfer are feasible. We have calculated the possibility of PT2 proton transfer, but starting geometries with PT2 all converged to conventional structures, ruling out this pathway. Thirdly, there is no definite trend in the order of the stability of conventional vs. proton-transferred structures. Finally, intra-pair proton transfer leads to the formation of rare tautomers, such as the 3H-keto–amino cytosine in 7HG·[C–H1]⁻_PT1.

Table 2 lists total energies and relative energies of all [G·C–H]⁻ conformers in the gas phase, computed using DFT, RI-MP2 and DLPNO-CCSD(T). Two different basis sets, 6-311++G(d,p) and aug-cc-pVQZ, were systematically employed in B3LYP calculations. The relative energies obtained with these two basis sets differ by 0.06 eV at most. We compared B3LYP and PWPB95 results using the aug-cc-pVQZ basis set, and the discrepancies in their relative energies are within 0.05 eV. The energies obtained at other levels of theory are very close to the B3LYP results. The order of the stability of 16 conformers remains nearly identical at all computational levels. We are therefore sure that the calculations reflect the intrinsic stabilities of different conformers.

The last column of Table 2 lists the B3LYP/DZP++ energies for [9HG·C–H]⁻ conformers calculated by Schaefer's group.[24] Compared to their work, we have considered both 9HG and 7HG tautomers for [G·C–H]⁻, and both conventional and intra-pair proton-transferred conformers were examined. As a result, we were able to identify many new structures and determined a new global minimum. Note that Schaefer et al. also calculated structures generated from deprotonating guanine C8–H, cytosine C5–H and C6–H, respectively. The C-deprotonated structures are much higher in energy than the N-deprotonated ones,[24] and thus are not discussed here.
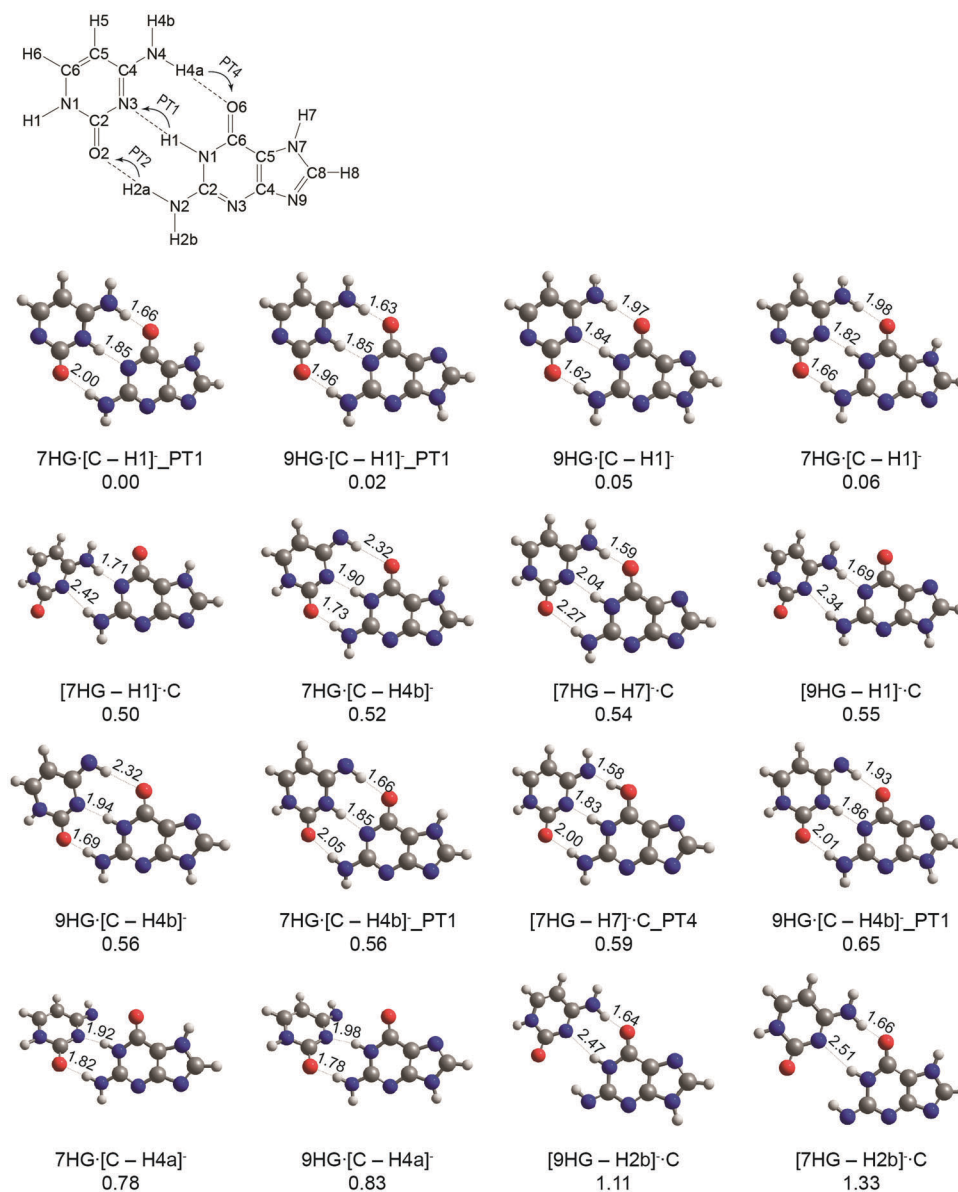
Fig. 2 Stable conformers of the [G·C–H]⁻ base pair. The ChemDraw structure presents the standard numbering scheme for Watson−Crick G·C and possible proton transfer pathways PT2, PT1 and PT4. Dashed lines indicate H-bonds, with bond distances shown in Å. Relative energies (eV, with respect to global minimum) were evaluated based on the sum of electronic energies calculated at the B3LYP/aug-cc-pVQZ//B3LYP/6-311++G(d,p) level with thermal correction (298 K) at B3LYP/6-311++G(d,p).

[9MG·C–H]⁻. The quantum chemical investigation was extended to identify stable conformations for gas-phase [9MG·C–H]⁻. Compared to free guanine, 9MG has few tautomerization and deprotonation sites, and we identified only eight conformers for [9MG·C–H]⁻. Their structures and energies are summarized in Fig. 3 and Table 3. [9MG–H]⁻ presents a similar trend in the relative stabilities of different conformations as that found for [G·C–H]⁻. The most stable conformation corresponds to a proton-transferred structure 9MG·[C–H1]⁻_PT1. Upon suggestion by the reviewer, we carried out additional calculations to explore the influence of water solvation on the conformational landscape of [9MG·C–H]⁻. All conformers were re-optimized in

water using the B3LYP/PCM/6-311++G(d,p) model, and the results are included in the last column of Table 3. The two lowest-energy conformers remain the same in aqueous solution with only a slight change in relative populations, i.e. 9MG·[C–H1]⁻_PT1 : 9MG·[C–H1]⁻ = 47 : 53 in water vs. 70 : 30 in the gas phase. 9MG·[C–H1]⁻_PT2 converged to 9MG·[C–H1]⁻ in solution, and the remaining conformers follow a nearly identical order of stability as in the gas phase. It can therefore be concluded that [9MG·C–H]⁻ shares a similar conformational landscape in the difference phases.

To examine the effects of deprotonation on the structures of base pairs, two dihedral angles G(C6–C2)–C(C2–C4) and

This journal is © the Owner Societies 2016

Phys. Chem. Chem. Phys., 2016, 18, 32222–32237 | 32227

Table 2 Total energies (E) and relative energies (ΔE) of [G·C–H]$^-$ at 298 K

		B3LYP/aug-cc-pVQZ		B3LYP/6-311++G(d,p)		M06-2X/def2-QZVPPD		RI-MP2/aug-cc-pVTZ	
Structures		E^a (Hartree)	ΔE (eV)	E^a (Hartree)	ΔE (eV)	E^a (Hartree)	ΔE (eV)	E^a (Hartree)	ΔE (eV)
1	7HG·[C–H1]$^-$_PT1	−937.2036728	0.00	−937.050376	0.00	−936.871297	0.00	−935.1702488	0.00
2	9HG·[C–H1]$^-$_PT1	−937.2029933	0.02	−937.0500226	0.01	−936.8710951	0.01	−935.1682914	0.05
3	9HG·[C–H1]$^-$	−937.2020146	0.05	−937.0491898	0.03	−936.8704547	0.02	−935.1678991	0.06
4	7HG·[C–H1]$^-$	−937.2012868	0.06	−937.0479996	0.06	−936.8689879	0.06	−935.1677362	0.07
5	[7HG–H1]$^-$·C	−937.1852988	0.50	−937.0316741	0.51	−936.8519811	0.53	−935.150415	0.54
6	7HG·[C–H4b]$^-$	−937.1846445	0.52	−937.0313121	0.52	−936.852381	0.51	−935.1506107	0.53
7	[7HG–H7]$^-$·C	−937.1837352	0.54	−937.0302913	0.55	−936.8516138	0.54	−935.1517722	0.50
8	[9HG–H1]$^-$·C	−937.1834462	0.55	−937.030306	0.55	−936.8508411	0.56	−935.1475056	0.62
9	9HG·[C–H4b]$^-$	−937.1831542	0.56	−937.0303146	0.55	−936.851515	0.54	−935.1483262	0.60
10	7HG·[C–H4b]$^-$_PT1	−937.1830053	0.56	−937.0305639	0.54	−936.8517514	0.53	−935.1515236	0.51
11	[7HG–H7]$^-$·C_PT4	−937.1820307	0.59	−937.027461	0.62	−936.8525049	0.51	−935.15143	0.51
12	9HG·[C–H4b]$^-$_PT1	−937.1797951	0.65	−937.0277184	0.62	−936.8490412	0.61	−935.1469886	0.63
13	7HG·[C–H4a]$^-$	−937.174833	0.78	−937.0199676	0.83	−936.842263	0.79	−935.1404223	0.81
14	9HG·[C–H4a]$^-$	−937.1730297	0.83	−937.018741	0.86	−936.8410246	0.82	−935.1376557	0.89
15	[9HG–H2b]$^-$·C	−937.1629029	1.11	−937.0082643	1.15	−936.8278532	1.18	−935.1217833	1.32
16	[7HG–H2b]$^-$·C	−937.1547370	1.33	−936.9992094	1.39	−936.8184293	1.44	−935.1129974	1.56

		PWPB95/aug-cc-pVQZ		DLPNO-CCSD(T)/aug-cc-pVTZ		B3LYP/DZP++	
Structures		E^a (Hartree)	ΔE (eV)	E^a (Hartree)	ΔE (eV)	$E_{ele}{}^b$ (Hartree)	ΔE (eV)
1	7HG·[C–H1]$^-$_PT1	−936.7482152	0.00	−935.3338762	0.00	—	—
2	9HG·[C–H1]$^-$_PT1	−936.74711	0.03	−935.333295	0.02	—	—
3	9HG·[C–H1]$^-$	−936.7462587	0.05	−935.3323383	0.04	−937.17994	0.00
4	7HG·[C–H1]$^-$	−936.7457728	0.07	−935.3311837	0.07	—	—
5	[7HG–H1]$^-$·C	−936.7302299	0.49	−935.3148225	0.52	—	—
6	7HG·[C–H4b]$^-$	−936.7299575	0.50	−935.3164845	0.47	—	—
7	[7HG–H7]$^-$·C	−936.7289756	0.52	−935.3150635	0.51	−937.16123	0.51
8	[9HG–H1]$^-$·C	−936.7282565	0.54	−935.3132765	0.56	−937.15951	0.56
9	9HG·[C–H4b]$^-$	−936.7287239	0.53	−935.3152479	0.51	−937.16028	0.53
10	7HG·[C–H4b]$^-$_PT1	−936.7295102	0.51	−935.3173011	0.45	—	—
11	[7HG–H7]$^-$·C_PT4	−936.727519	0.56	−935.3158243	0.49	—	—
12	9HG·[C–H4b]$^-$_PT1	−936.725923	0.61	−935.3143115	0.53	—	—
13	7HG·[C–H4a]$^-$	−936.7206106	0.75	−935.3063585	0.75	—	—
14	9HG·[C–H4a]$^-$	−936.7187348	0.80	−935.3047327	0.79	−937.14825	0.86
15	[9HG–H2b]$^-$·C	−936.7062182	1.14	−935.2892135	1.22	−937.13695	1.17
16	[7HG–H2b]$^-$·C	−936.6976163	1.38	−935.2797923	1.47	—	—

^{a} Absolute gas-phase energy, defined as the sum of electronic energies at the specified level of theory and B3LYP/6-311++G(d,p) thermal correction at 298 K. ^{b} Ref. 24, electronic energy only; relative energy was calculated with respect to 9HG·[C–H1]$^-$ without thermal correction.

G(C6–N1)–C(N3–C4) were calculated for [GC–H]$^-$ and [9MG–H]$^-$ at their B3LYP/6-311++G(d,p) geometries. The results are listed in Table 4, for comparison with neutral G·C and 9MG·C which bear perfect planar symmetry. Deprotonation of cytosine H4a results in the largest perturbation to this planarity, followed by deprotonation of cytosine H4b. Base pairs undergo less dramatic geometrical changes upon deprotonation of guanine N7–H (or N9–H for 9HG) or cytosine N1–H; in all of which the distortions of dihedral angles are less than 11°. 9-Methylation of guanine has a minor influence on H-bonds, geometrical structures and relative stabilities of base pairs. This is true for both neutral and deprotonated base pairs.

3.2 Anomalous CID of [G·C–H]$^-$ and [9MG·C–H]$^-$

[G·C–H]$^-$ + Xe. Fig. 4a shows a representative CID mass spectrum for [G·C–H]$^-$ + Xe at E_{col} = 2.0 eV. Product ions are observed at m/z 110 and 150 over the center-of-mass E_{col} range of 0.1–5.0 eV, corresponding to the dissociation of the parent ion into [C–H]$^-$ and [G–H]$^-$, respectively. This indicates that both the conventional and the proton-transferred structures of [G·C–H]$^-$ exist in the gas phase. What is striking about the CID result is that the abundance of [G–H]$^-$ is overwhelmingly higher than that of [C–H]$^-$. Fig. 4b plots the ratio of [G–H]$^-$ vs. [C–H]$^-$ as a function of E_{col}. The ratio is up to 85 at 1.5 eV, decreases as E_{col} increases, and becomes energy-independent (∼22) at E_{col} > 2.5 eV.

Cross sections for [G–H]$^-$ and [C–H]$^-$ are plotted in Fig. 5a and b. For collisions above a few eV, long range forces are negligible, so the hard sphere cross section (σ_{HS} = ∼120 Å^2 for [G·C–H]$^-$ + Xe) can be taken as a reasonable estimate of the maximum collision cross section. At sufficiently high energies, we expected that every hard sphere collision would lead to dissociation; therefore, the total CID cross section should approach σ_{HS} and becomes independent of E_{col}. In contrast, the sum of [G–H]$^-$ and [C–H]$^-$ cross sections (not shown here) shows a sign of leveling off at 1.8 eV, and starts to decrease afterwards. This discrepancy is an artifact due to the loss of sideways-scattered product ions, to be rationalized below.
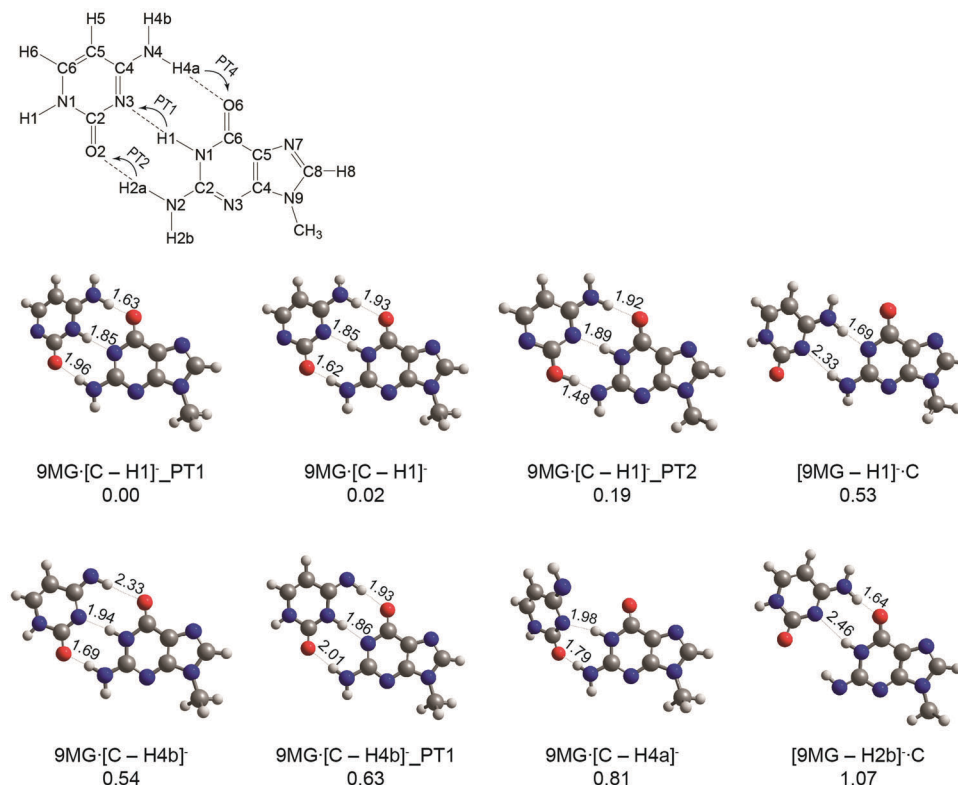
Fig. 3   Stable conformers of the [9MG·C−H]⁻ base pair. The ChemDraw structure presents the standard numbering scheme for Watson−Crick 9MG·C and possible proton transfer pathways PT2, PT1 and PT4. Dashed lines indicate H-bonds, with bond distances shown in Å. Relative energies (eV, with respect to global minimum) were evaluated based on the sum of electronic energies calculated at the B3LYP/aug-cc-pVQZ//B3LYP/6-311++G(d,p) level with thermal correction (298 K) at B3LYP/6-311++G(d,p).

Table 3   Total energies (E) and relative energies (ΔE) of [9MG·C−H]⁻ at 298 K

Structures		B3LYP/aug-cc-pVQZ		B3LYP/6-311++G(d,p)		M06-2X/def2-QZVPPD	
		E^a (Hartree)	ΔE (eV)	E^a (Hartree)	ΔE (eV)	E^a (Hartree)	ΔE (eV)
1	9MG·[C−H]⁻_PT1	−976.4996609	0.00	−976.3401518	0.00	−976.1486035	0.00
2	9MG·[C−H]⁻	−976.4988595	0.02	−976.3395233	0.02	−976.148205	0.01
3	9MG·[C−H]⁻_PT2	−976.4927562	0.19	−976.3330058	0.19	−976.144559	0.11
4	[9MG−H1]⁻·C	−976.4800204	0.53	−976.3203564	0.54	−976.1283241	0.55
5	9MG·[C−H4b]⁻	−976.4798869	0.54	−976.3205231	0.53	−976.1291607	0.53
6	9MG·[C−H4b]⁻_PT1	−976.4763454	0.63	−976.3176912	0.61	−976.1264619	0.60
7	9MG·[C−H4a]⁻	−976.4697578	0.81	−976.3089483	0.85	−976.1186187	0.82
8	[9MG−H2b]⁻·C	−976.4601585	1.07	−976.2990641	1.12	−976.1060179	1.16

Structures		RI-MP2/aug-cc-pVTZ		PWPB95/aug-cc-pVQZ		DLPNO-CCSD(T)/aug-cc-pVTZ		B3LYP/PCM/6-311++G(d,p)	
		E^a (Hartree)	ΔE (eV)	E^a (Hartree)	ΔE (eV)	E^a (Hartree)	ΔE (eV)	E^b (Hartree)	ΔE (eV)
1	9MG·[C−H1]⁻_PT1	−974.3599979	0.00	−976.0164273	0.00	−974.5409049	0.00	−976.4330238	0.00
2	9MG·[C−H1]⁻	−974.3599032	0.00	−976.0158843	0.01	−974.5401759	0.02	−976.4331415	0.00
3	9MG·[C−H1]⁻_PT2	−974.3543335	0.15	−976.0096337	0.18	−974.5355155	0.15	Converge to structure 2	
4	[9MG−H1]⁻·C	−974.3391574	0.57	−975.9972422	0.52	−974.5208736	0.55	−976.4258897	0.20
5	9MG·[C−H4b]⁻	−974.3402035	0.54	−975.9980839	0.50	−974.5231084	0.48	−976.4180947	0.41
6	9MG·[C−H4b]⁻_PT1	−974.3386188	0.58	−975.9946593	0.59	−974.52185	0.52	−976.4186918	0.39
7	9MG·[C−H4a]⁻	−974.329506	0.83	−975.9877398	0.78	−974.512643	0.77	−976.4145867	0.50
8	[9MG−H2b]⁻·C	−974.31403	1.25	−975.9769379	1.07	−974.497699	1.18	−976.4126945	0.56

^{a} Absolute gas-phase energy, defined as the sum of electronic energies at the specified level of theory and B3LYP/6-311++G(d,p) thermal correction at 298 K. ^{b} Absolute energy in aqueous solution, defined as the sum of electronic energies and 298 K thermal correction at B3LYP/PCM/6-311++G(d,p).

Because of the distribution in collision energy, the experimental cross sections for product ions increase from zero before the true dissociation thresholds. To extract true thresholds, the E_{col} dependence of the cross section was fit using a "true" $\sigma(E)$

Table 4 Dihedral angles of neutral and deprotonated base pairs

Structures		G(C6–C2)–C(C2–C4)	G(C6–N1)–C(N3–C4)	Structures		9MG(C6–C2)–C(C2–C4)	9MG(C6–N1)–C(N3–C4)
	7HG·C	−1.8	−2.5				
	9HG·C	0.0	0.0	9MG·C		0.8	1.1
1	7HG·[C–H1]⁻_PT1	−8.4	−10.7				
2	9HG·[C–H1]⁻_PT1	−7.7	−9.8	1	9MG·[C–H1]⁻_PT1	−7.6	−9.7
3	9HG·[C–H1]⁻	−8.7	−5.8	2	9MG·[C–H1]⁻	−8.6	−5.8
				3	9MG·[C–H1]⁻_PT2	2.2	−0.1
4	7HG·[C–H1]⁻	−10.1	−7.4				
5	[7HG–H1]⁻·C	−9.0	−17.4				
6	7HG·[C–H4b]⁻	−12.0	−12.6				
7	[7HG–H7]⁻·C	−5.5	−9.0				
8	[9HG–H1]⁻·C	−8.4	−16.3	4	[9MG–H1]⁻·C	−8.5	−16.3
9	9HG·[C–H4b]⁻	−9.2	−9.5	5	9MG·[C–H4b]⁻	−9.5	−9.8
10	7HG·[C–H4b]⁻_PT1	−12.5	−15.9				
11	[7HG–H7]⁻·C_PT4	−6.2	−9.0				
12	9HG·[C–H4b]⁻_PT1	−12.8	−16.1	6	9MG·[C–H4b]⁻_PT1	−12.6	−15.9
13	7HG·[C–H4a]⁻	43.9	34.3				
14	9HG·[C–H4a]⁻	44.1	32.6	7	9MG·[C–H4a]⁻	−44.2	−32.6
15	[9HG–H2b]⁻·C	0.0	0.0	8	[9MG–H2b]⁻·C	0.0	0.0
16	[7HG–H2b]⁻·C	0.0	0.0				
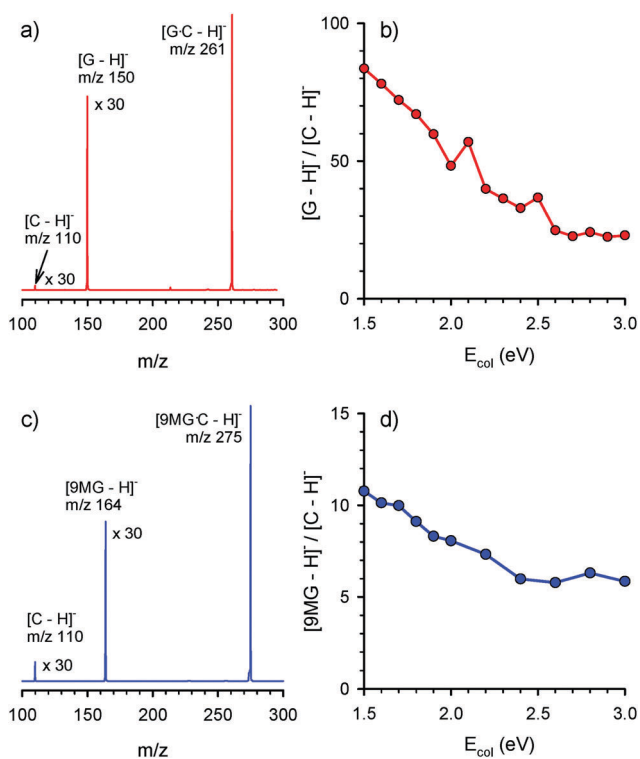
Fig. 4 CID mass spectra (measured at E_{col} = 2.0 eV) and product branching ratio as a function of E_{col} for (a and b) [G·C–H]⁻ + Xe and (c and d) [9MG·C–H]⁻ + Xe.

Fig. 5 CID product ion cross sections for (a and b) [G·C–H]⁻ + Xe and (c and d) [9MG·C–H]⁻ + Xe.

function generated from the modified line-of-center (LOC) model and including the contributions from reactant vibrational and rotational energies[25,61,62]

$$\sigma(E) = \sigma_0 \frac{(E_{col} + E_{vib} + E_{rot} - E_0)^n}{E_{col}} \quad (1)$$

for $(E_{col} + E_{vib} + E_{rot}) > E_0$; otherwise, $\sigma(E) = 0$. Here σ_0 is an energy-independent normalization constant, E_{vib} and E_{rot} are the

vibrational and rotational energies of reactant ions, E_0 is the dissociation threshold, and n is a fitting parameter used to adjust the slope of $\sigma(E_{col})$ (equal to 1.0 in the canonical LOC model). The key assumption is that at near-threshold collision energies, at least some fraction of collisions are completely inelastic and all E_{col} is converted into internal energy to drive CID. Note that this assumption was verified in threshold CID measurements for a wide variety of ions,[25] and it is appropriate for the current systems based on the comparison of the fitting

32230 | *Phys. Chem. Chem. Phys.*, 2016, **18**, 32222–32237

This journal is © the Owner Societies 2016

results and the calculated thresholds; but it may not always be true, such as in CID of Al_6 by rare gas.[63,64]

To fit experimental data, $\sigma(E)$ was convoluted with experimental broadening functions, including those from primary ion beam and target gas velocities and ion vibrational and rotational energies. The fitting was done using the program of Anderson *et al.*[65] For Xe atoms, a Maxwell–Boltzmann distribution of velocities at 300 K was used. For the primary ion beam of [G·C–H]$^-$, we used RPA measured kinetic energy distribution (fitted by an asymmetric Lorentzian function), and assumed a Maxwell–Boltzmann distribution of E_{rot} at 310 K. E_{vib} of [G·C–H]$^-$ was sampled using the following probability distribution

$$P(E_{vib}) = \frac{(E_{vib})^{1/2} \times \exp\left(\frac{-E_{vib}}{2 E_{vib\_peak}}\right)}{(E_{vib\_peak})^{1/2} \times \exp(-0.5)} \quad (2)$$

where E_{vib_peak} is the most probable vibrational energy of the Boltzmann distribution by summing over the partition function. $\sigma(E)$ was run through a Monte Carlo simulation that included all experimental broadening factors. For each E_{col}, the simulation sampled 100 000 ion-molecule collisions, thereby building up a simulated cross section for direct comparison with the ion-beam experiment. The rising curvature and the overall profile of $\sigma(E)$ depend mostly on E_0. A leveling-off collision energy was used in the fitting so that the simulated $\sigma(E)$ would not exceed σ_{HS} at high E_{col}. Due to the large number of vibrational models in [G·C–H]$^-$, kinetic shifts in the threshold may be expected in that E_{col} in excess of the dissociation limit was required to drive CID on the experimental timescale ($\sim$500 μs).[66] In the fitting we used the RRKM model to decide whether each sample led to detectable dissociation or not.

The black plots in Fig. 5a and b show the convoluted $\sigma(E)$ for the two CID channels of [G·C–H]$^-$ + Xe, with the fit E_0 indicated by arrows. The best fit E_0 is 1.61 eV for [G·C–H]$^-$ → [G–H]$^-$ + C and 1.60 eV for [G·C–H]$^-$ → [C–H]$^-$ + G, and n is 1.60 and 1.40, respectively. For the [G–H]$^-$ product channel, the fit is reasonable up to 1.8 eV, after that the fitting deviates from the experimental cross section which may be explained by two facts. First, this might be taken as evidence of competition between two dissociation channels. This is consistent with the observation that the cross section for [G–H]$^-$ starts to decrease at 1.8 eV while that of [C–H]$^-$ continues to increase. Such interchannel competition is more clearly demonstrated in the E_{col} dependence of the product branching in Fig. 4b, albeit the absolute cross section of [C–H]$^-$ is still much lower than that of [G–H]$^-$ at high E_{col}. Secondly, CID tends to produce a large fraction of sideway-scattered product ions. The average speed of these sideway-scattered ions increases with E_{col}, such that they become increasingly difficult to collect, even using an ion guide.[62,67] The drop in ion collection efficiency at high E_{col} may contribute to the decrease of [G–H]$^-$ ions and explains why the total CID cross section drops when the system goes to the high E_{col} regime.

[9MG·C–H]$^-$ + Xe. One factor that complicates the data interpretation for [G·C–H]$^-$ dissociation is that there exist mixtures of 7HG and 9HG tautomers in the G·C pair. To this end, another set of CID was done using [9MG·C–H]$^-$, for which we need not worry about the possibilities for N9H–N7H tautomerization and deprotonation at guanine N7 and N9. The CID product ion mass spectrum and product branching for [9MG·C–H]$^-$ + Xe are presented in Fig. 4c and d. Product ions are observed at m/z 110 and 164, corresponding to [C–H]$^-$ and [9MG–H]$^-$, respectively. Here again, anomalous dissociation was observed – the product channel of [9MG–H]$^-$ + C predominates over that of [C–H]$^-$ + 9MG. Cross sections for the two channels are presented in Fig. 5c and d, and their E_{col} dependence was simulated in a way similar to that used for [G·C–H]$^-$. The fit E_0 = 1.74 eV and n = 1.90 for [9MG·C–H]$^-$ → [9MG–H]$^-$ + C *vs.* E_0 = 1.68 eV and n = 1.10 for [9MG·C–H]$^-$ → [C–H]$^-$ + 9MG.

In the modified LOC fitting of CID cross sections, the physical significance of the n parameter greater than 1 depends on the CID mechanism assumed. For example, it has been shown that a statistical theory based on reverse three-body recombination in a long-lived complex can lead to n values greater than unity.[68] However, a complex-mediated model is less likely for [G·C–H]$^-$ (or [9MG·C–H]$^-$) + Xe since their binding energy is negligible compared to available E_{col}. It has also been shown that for a translationally driven reaction that involves a rate-limiting TS, different curvatures are possible depending on the properties of the TS.[69] Because the limiting fact in CID is more related to translation-to-vibrational energy transfer in initial collision, this theory is not applicable, either. Alternatively, it has been shown that an orientation-dependent activation barrier results in a quadratic threshold law with n = 2 for endoergic reactions under a LOC model.[61] The dissociation energies of base pairs are obviously not angle-dependent, but it would not be surprising if the translation-to-vibrational energy transfer and thus the CID probability are collision orientation dependent. This is indeed exactly what should be anticipated for our CID experiment since the base pairs have flat geometries and their interaction with Xe is largely anisotropic.

An obvious question concerning the two sets of CID is how the guanine 9-methylation affects product distribution. Insight into this issue was provided by CID cross sections. While the 9-methyl substitution does not grossly change CID results, the maximum cross section for product ion [9MG–H]$^-$ decreases by one third as compared to [G·C–H]$^-$ → [G–H]$^-$ + C; in the meantime the maximum cross section for [C–H]$^-$ increases by a factor of 2. Changes in product distributions can be more clearly viewed in terms of branching ratios in Fig. 4. The deprotonated guanine fragment dominates in both [G·C–H]$^-$ + Xe and [9MG·C–H]$^-$ + Xe, but it grows much more overwhelming in the first system.

3.3 Statistical interpretation of intra-base-pair proton transfer and dissociation

Table 5 lists B3LYP calculated dissociation energies E_0 for all [G·C–H]$^-$ and [9MG·C–H]$^-$ conformers to their ionic and neutral nucleobases, which may be interpreted as base pair interaction energies. [G·C–H]$^-$ has much higher interaction energy than neutral G·C (1.18 eV at B3LYP/DZP++[70] and 1.24 eV at

This journal is © the Owner Societies 2016

Phys. Chem. Chem. Phys., 2016, **18**, 32222–32237 | **32231**

Table 5 B3LYP calculated dissociation thresholds (E_0) of deprotonated base pairs

Structures		E_0 (eV) 6-311++G(d,p)	aug-cc-pVQZ	Structures		E_0 (eV) 6-311++G(d,p)	aug-cc-pVQZ
1	7HG·[C–H1]⁻_PT1	1.57	1.56				
2	9HG·[C–H1]⁻_PT1	1.67	1.66	1	9MG·[C–H1]⁻_PT1	1.68	1.67
3	9HG·[C–H1]⁻	1.64	1.64	2	9MG·[C–H1]⁻	1.62	1.62
				3	9MG·[C–H1]⁻_PT2	1.21	1.21
4	7HG·[C–H1]⁻	1.60	1.59				
5	[7HG–H1]⁻·C	0.76	0.76				
6	7HG·[C–H4b]⁻	1.26	1.24				
7	[7HG–H7]⁻·C	0.74	0.76				
8	[9HG–H1]⁻·C	0.84	0.83	4	[9MG–H1]⁻·C	0.84	0.83
9	9HG·[C–H4b]⁻	1.25	1.23	5	9MG·[C–H4b]⁻	1.23	1.21
10	7HG·[C–H4b]⁻_PT1	0.88	0.86				
11	[7HG–H7]⁻·C_PT4	2.76	2.71				
12	9HG·[C–H4b]⁻_PT1	0.92	0.90	6	9MG·[C–H4b]⁻_PT1	0.92	0.90
13	7HG·[C–H4a]⁻	1.21	1.19				
14	9HG·[C–H4a]⁻	1.19	1.17	7	9MG·[C–H4a]⁻	1.16	1.14
15	[9HG–H2b]⁻·C	0.43	0.44	8	[9MG–H2b]⁻·C	0.43	0.44
16	[7HG–H2b]⁻·C	0.38	0.38				

CCSD(T)//MP2 with complete basis set calculation),[71] because of the increased dipole interaction in [G·C–H]⁻. According to the conformation search in Section 3.1, the most likely conformers of [G·C–H]⁻ are 7HG·[C–H1]⁻ and 9HG·[C–H1]⁻ and their proton-transferred isomers, and those of [9MG·C–H]⁻ are 9MG·[C–H1]⁻ and its proton-transferred isomer. Therefore, we focus on the dissociation of these six structures.

Dissociation of 7HG·[C–H1]⁻ and 7HG·[C–H1]⁻_PT1. Let us first look at the reaction PES of 7HG·[C–H1]⁻ and its proton-transferred isomer in Fig. 6a. The energies of the two conformers and their interconversion barrier as well as their dissociation thresholds are the most important quantities for examining the interplay of intra-base-pair proton transfer and dissociation. Therefore these values were calculated at different levels of theory and with a range of basis sets, as presented in the figure. There is an overall good agreement between the energies calculated using different methods and the energy measured in CID. The B3LYP/aug-cc-pVQZ method was found to give acceptable representation of the reaction PES, with an accuracy estimated to be within 0.1 eV. For consistency, we used B3LYP/aug-cc-pVQZ energies in all the kinetic analyses.

Using RRKM theory, we have estimated the rate constant for 7HG·[C–H1]⁻ → TS → 7HG·[C–H1]⁻_PT1 under experimental conditions. Vibrational frequencies and rotational constants for the reactant and the TS were derived from B3LYP/6-311++G(d,p) results. The rotation quantum number K was treated as active in evaluating the rate $k(E, J)$ so that all $(2J + 1)$ K-levels are counted,[72] i.e.

$$k(E, J) = \frac{d}{h} \frac{\sum_{K=-J}^{J} G[E - E_0 - E_r^\dagger(J, K)]}{\sum_{K=-J}^{J} N[E - E_r(J, K)]} \quad (3)$$

where d is the reaction path degeneracy, G is the sum of accessible states from 0 to $E - E_0 - E_r^\dagger$ in the TS, N is the energized reactant's density of states, E is the system energy, E_0 is the activation energy or unimolecular dissociation threshold,

and E_r and $E_r^\dagger$ are the rotational energies for the reactant and the TS, respectively.

The forward activation barrier for intra-pair proton transfer from 7HG·[C–H1]⁻ is only 0.06 eV. Accordingly, the rate constant for the forward reaction falls within the range of 0.72–1.04×10^{12} s⁻¹ at $E_{col} = 2.0$–3.0 eV. This rate is high enough for 7HG·[C–H1]⁻_PT1 to be formed in collisions. The reverse reaction from 7HG·[C–H1]⁻_PT1 to 7HG·[C–H1]⁻ proceeds with a lower rate constant of 0.32–0.56×10^{12} s⁻¹ in the same energy range. Interconversion between 7HG·[C–H1]⁻ and 7HG·[C–H1]⁻_PT1 occurs on a time-scale of ps, which is significantly shorter than the dissociation timescale. Therefore, during CID a new thermodynamical equilibrium was established for eqn (4):

$$7HG\cdot[C–H1]^- \rightleftharpoons 7HG\cdot[C–H1]^-\_PT1 \quad (4)$$

The equilibrium constant K_{PT} for eqn (4) is E_{col}-dependent, and calculated to be 1.9–2.3 at $E_{col} = 2.0$–3.0 eV. The facile intra-base-pair proton transfer was confirmed in a direct-dynamics trajectory study of 7HG·[C–H]⁻ + ¹O₂ at $E_{col} = 0.1$ eV. Trajectories were calculated using the Venus program of Hase et al.[73,74] to set up initial conditions, and the Hessian-based predictor-corrector algorithm of Schlegel et al.[75] to integrate trajectories at B3LYP/6-31G(d). While the major purpose of the trajectory simulation was to examine oxidation dynamics of 7HG·[C–H1]⁻, a large fraction of the trajectories did not have reaction with ¹O₂. Of these non-reactive trajectories, 32% underwent proton transfer via the PT1 pathway, and 20% of the proton transfer is in fact reversible and re-crossed the TS.

Two dissociation asymptotes eqn (5) and (6), which originate from 7HG·[C–H1]⁻ and 7HG·[C–H1]⁻_PT1, respectively, are shown in Fig. 6a. Dissociation of 7HG·[C–H1]⁻_PT1 produces a 3H-keto–amino tautomer of cytosine (see C_6 in Fig. S4, ESI†). Calculated thresholds for eqn (5) and (6) are close to the experimentally fit values in Fig. 5. Note that the threshold for eqn (5) is systematically higher than that for eqn (6) by 0.02–0.04 eV at all computational levels.
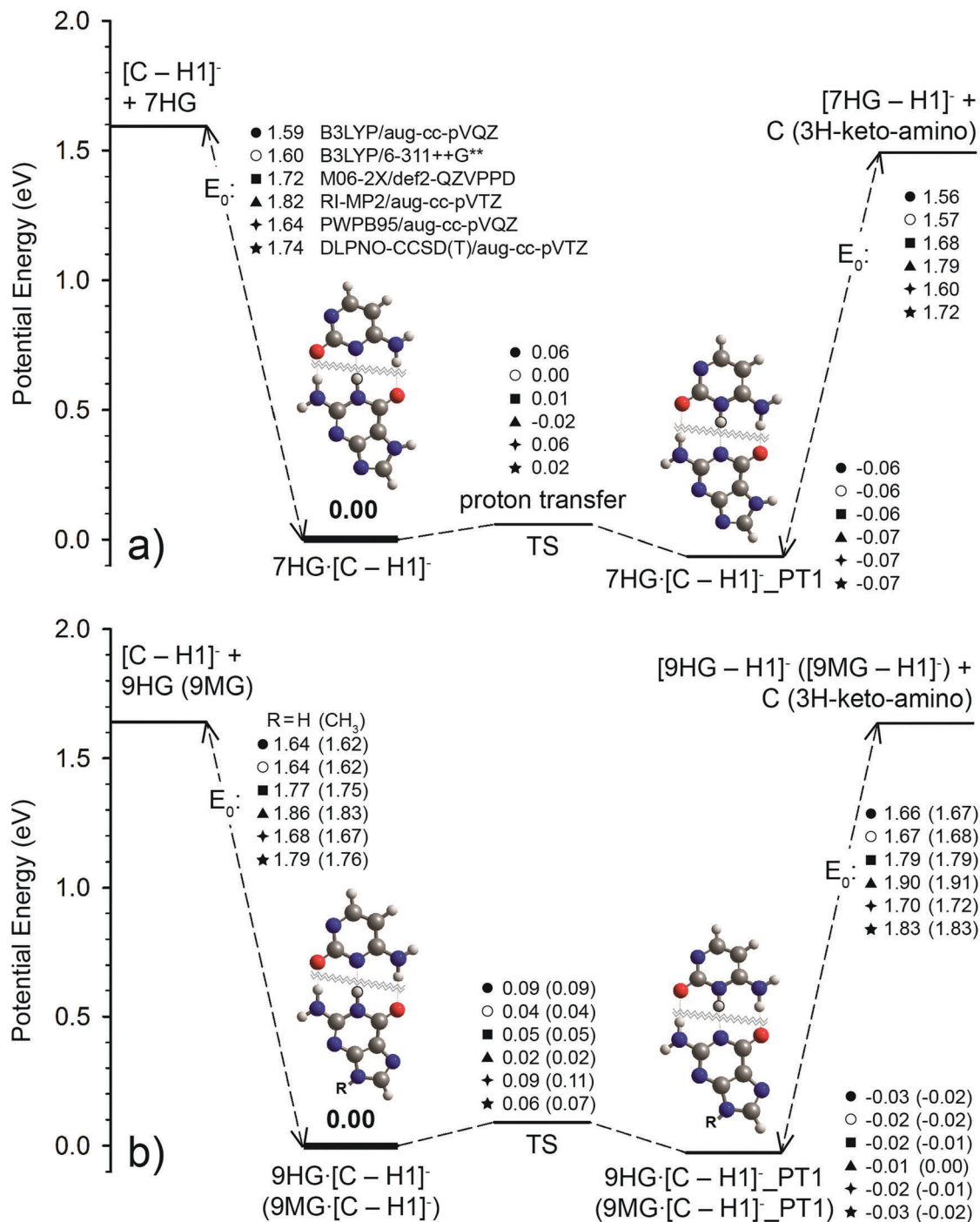
Fig. 6 Schematic reaction coordinates for intra-base-pair proton transfer and dissociation of (a) 7HG·[C−H]⁻, and (b) 9HG·[C−H]⁻ and 9MG·[C−H]⁻ (indicated in parentheses). Energies were calculated at various levels of theory as indicated, including thermal corrections at 298 K.

$$7HG \cdot [C-H1]^- \rightarrow 7HG + [C-H1]^- \quad E_0 = 1.59 \text{ eV} \quad (5)$$

$$7HG \cdot [C-H1]^-\_PT1 \rightarrow [7HG-H1]^- + C(3H-keto-amino)$$

$$E_0 = 1.56 \text{ eV} \quad (6)$$
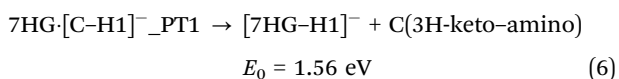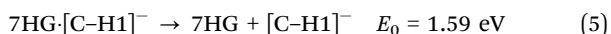
Since no reverse activation barriers could be located for eqn (5) and (6), vibrational frequencies appropriate for dissociation TSs had to be assumed for RRKM modeling. A TS estimate was made, which consists of the frequencies that are partitioned into the two products with little changes and thus termed conserved mode[76] and the remaining that correspond to the relative motion of the two products and thus termed transitional modes.[76] The frequencies of the six translational modes lost upon dissociation were chosen from the base pair. A stretching frequency of the H-bonds was chosen as the reaction coordinate and removed. The five remaining frequencies (corresponding to

This journal is © the Owner Societies 2016

Phys. Chem. Chem. Phys., 2016, **18**, 32222–32237 | **32233**

bending, torsion, sliding and scissoring of the two nucleobases with respect to each other), which became intermolecular motions of dissociated products, were scaled by a factor of 0.5 to reflect the looseness of TSs that changes the activation entropy. A similar scaling factor was used by Armentrout's group to assign the transitional modes in dissociation of energized metal ion-ligand complex ML_x.[77–79] The fact that such scaled translational frequencies were successfully used to extract dissociation energies of ML_x suggests that this scaling factor yields appropriate "loose" TSs corresponding to weak associations of products. Using "loose" TSs, we estimated that the dissociation rate constants k_{diss} for eqn (5) and (6) are within the range of $10^4–10^5$ s^{-1} at $E_{col} \geq 2.0$ eV.

Note that the tightness of TSs might affect rate constants. However, eqn (5) and (6) have similar mechanisms and thresholds. Thus the uncertainty of k_{diss} calculations associated with the choice of TSs may be similar for the two dissociation asymptotes, and tends to cancel when calculating the ratio of k_{diss} for eqn (5) and (6). Table 6 summarizes RRKM results. The branching ratio of "[7HG–H]$^-$ + C" to "[C–H]$^-$ + 7HG" was determined by the product of K_{PT} and k_{diss}(7HG·[C–H1]$^-$)/k_{diss}(7HG·[C–H1]$^-$_PT1). That is 22 at 2.0 eV, 7.39 at 2.5 eV and 4.72 at 3.0 eV. RRKM product distributions qualitatively agree with the experiment, including the dominance of deprotonated guanine product ions in the entire E_{col} range and the decrease of its branching as E_{col} increases.

Dissociation of 9HG·[C–H1]$^-$ and 9HG·[C–H1]$^-$_PT1. Reaction pathways for these two structures can be summarized as:

$$9HG\cdot[C\text{–}H1]^- \rightleftharpoons 9HG\cdot[C\text{–}H1]^-\_PT1 \qquad (7)$$

$$9HG\cdot[C\text{–}H1]^- \rightarrow 9HG + [C\text{–}H1]^- \quad E_0 = 1.64 \text{ eV} \qquad (8)$$

$$9HG\cdot[C\text{–}H1]^-\_PT1 \rightarrow [9HG\text{–}H1]^- + C(3H\text{-keto–amino})$$
$$E_0 = 1.66 \text{ eV} \qquad (9)$$
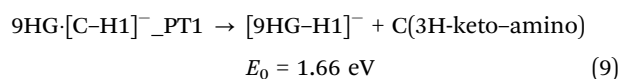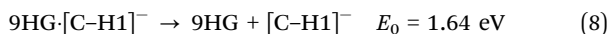
Table 6 RRKM-predicted proton transfer equilibrium constants (K_{PT}), ratio of dissociation rate constants (k_{diss}), and product branching

E_{col} (eV)	K_{PT}	k_{diss} (conventional)/ k_{diss} (PT structure)	Ratio of [G/9MG–H]$^-$/[C–H]$^-$	
			RRKM	Exp.
7HG·[C–H]$^-$ and 7HG·[C–H]$^-$_PT1 (total population 62.1%)				
2.0	2.28	9.65	22.0	—
2.5	2.03	3.64	7.39	—
3.0	1.86	2.54	4.72	—
9HG·[C–H]$^-$ and 9HG·[C–H]$^-$_PT1 (total population 37.9%)				
2.0	1.54	0.28	0.43	—
2.5	1.44	0.26	0.37	—
3.0	1.38	0.27	0.37	—
Ensemble average for [G·C–H]$^-$				
2.0	—	—	13.8	48.3
2.5	—	—	4.6	36.7
3.0	—	—	3.1	22.9
9MG·[C–H]$^-$ and 9MG·[C–H]$^-$_PT1 (total population 100%)				
2.0	1.27	0.10	0.13	8.1
2.5	1.22	0.17	0.21	5.9
3.0	1.18	0.22	0.26	5.9

The major difference between the reaction PES for 9HG·[C–H1]$^-$/9HG·[C–H1]$^-$_PT1 in Fig. 6b and their 7HG analogues in Fig. 6a is that the forward barrier for proton transfer from 9HG·[C–H1]$^-$ is 0.03 eV higher than that from 7HG·[C–H1]$^-$, while the reverse barriers are of the same energy in the two systems. In addition, the E_0 for dissociation of 9HG·[C–H1]$^-$_PT1 to [9HG–H]$^-$ (eqn (9)) is 0.02 eV higher than that of 9HG·[C–H1]$^-$ to [C–H]$^-$ (eqn (8)). This is opposite to the case of 7HG·[C–H1]$^-$/7HG·[C–H1]$^-$_PT1 where the E_0 to [G–H]$^-$ (eqn (6)) is 0.03 eV lower than that to [C–H]$^-$ (eqn (5)). As a result, RRKM predicted a distinctively different dissociation product distribution for 9HG·[C–H1]$^-$/9HG·[C–H1]$^-$_PT1, of which [9HG–H1]$^-$ accounts for at most less than one-third of the product ions. This clearly contradicts to the experimental CID data in Fig. 4b.

It should be borne in mind that CID measurements reflect averaged results of the four lowest-lying [G·C–H]$^-$ conformers, including 7HG·[C–H1]$^-$ and 7HG·[C–H1]$^-$_PT1 (total population 62.1% based on Boltzmann distribution at 298 K), and 9HG·[C–H1]$^-$ and 9HG·[C–H1]$^-$_PT1 (total population 37.9%). Interconversions between the conventional and the proton-transferred conformers resulted in new equilibria and changed relative populations of the two conformers. But the total population for (7HG·[C–H1]$^-$ + 7HG·[C–H1]$^-$_PT1) vs. (9HG·[C–H1]$^-$ + 9HG·[C–H1]$^-$_PT1) remained constant. Accordingly, we were able to estimate the ensemble-averaged RRKM product branching for [G·C–H]$^-$ by taking into account the populations of different tautomers, as listed in Table 6. The averaged product branching still qualitatively follows the experimental trend. This is because the "different product distribution" of 9HG·[C–H1]$^-$/9HG·[C–H1]$^-$_PT1 is masked due to their small weight in averaging. This of course raises questions about the validity of the RRKM prediction and thus the underlying statistical assumption for [G·C–H]$^-$.

Dissociation of 9MG·[C–H1]$^-$ and 9MG·[C–H1]$^-$_PT1. Gas-phase [9MG·C–H]$^-$ can be well represented by a conventional and a proton-transferred structure of 9MG·[C–H1]$^-$. 9MG·[C–H1]$^-$/9MG·[C–H1]$^-$_PT1 has similar proton transfer barriers and dissociation asymptotes as those for 9HG·[C–H1]$^-$/9HG·[C–H1]$^-$_PT1. We therefore combined the PESs for the two systems in Fig. 6b.

Similar to 9HG·[C–H1]$^-$/9HG·[C–H1]$^-$_PT1, RRKM product branching for 9MG·[C–H1]$^-$/9MG·[C–H1]$^-$_PT1 is just opposite to the experimental measurement. The RRKM ratio of "[9MG–H]$^-$ + C" to "[C–H]$^-$ + 9MG" is 0.13 at E_{col} = 2.0 eV, 0.21 at 2.5 eV, and 0.26 at 3.0 eV. They are smaller by a factor of 62, 28 and 23, respectively, than the corresponding experimental values. RRKM predicts more substantial formation and/or dissociation of 9MG·[C–H1]$^-$_PT1. RRKM rate constants were calculated using harmonic frequencies of reactants and TSs, and assumed "loose" TSs for dissociation, which may introduce artifacts. However, a correction of two orders of magnitude to RRKM branching is unusual. It implies that reactions of 9MG·[C–H1]$^-$ and 9MG·[C–H1]$^-$_PT1 do not follow the minimum energy pathways in Fig. 6b, and exhibit significant non-statistical kinetics. This is reminiscence of the discrepancy we have observed in the experimental product distribution of [G·C–H]$^-$ vs. the RRKM product branching for

32234 | Phys. Chem. Chem. Phys., 2016, **18**, 32222–32237

This journal is © the Owner Societies 2016

9HG·[C–H1]⁻/9HG·[C–H1]⁻_PT1. It leads us to believe that non-RRKM kinetics exists for both [9HG·C–H]⁻ and [9MG·C–H]⁻.

Understanding the origin of non-statistical kinetics is challenging, and thus has potential to provide insight into the less intuitive aspects of the deprotonated base pair chemistry. There are three stages during which non-statistical behavior may possibly initiate. The first one is the TS crossing stage for intra-pair proton transfer. We noticed that the distance from G(N1) to C(N3) in the proton transfer TSs is shortened by 0.3 Å. To accommodate the dramatic decrease of G(N1)–C(N3) and meanwhile maintain the other two H-bonds, TSs have to twist to a geometry with the dihedral angle G(C6–C2)–C(C2–C4) = −24°. This may bring about a dynamic bottleneck along the constrained configuration and implies that proton-transfer dynamics may be more complicated than what was suggested by the calculated PESs. Indeed, we have observed TS re-crossing in proton transfer trajectories of 7HG·[C–H1]⁻. The second stage deals with a critical configuration that separates the base pair and the dissociation products. A trajectory is free to move through all reactant phase space, but once it crosses the critical configuration, it never returns to the reactant region. So the critical configuration represents a dividing surface between the reactant and product regions of the phase space. For intra-pair proton transfer that has a well-defined saddle point (*i.e.* TS), it is an accurate enough approximation to fix the dividing surface at the saddle point.[80] A problem arose in base pair dissociation for which there is no reverse barrier and the location of the dividing surface depends on energy.[80] An approximate approach of "loose" TSs was employed in the interpretation of base pair dissociation kinetics, as others have used in similar situations.[77–79] However, a more rigorous way to treat such dissociation is to locate the critical configuration in reaction trajectories or use variational unimolecular rate theory.[76,80] Finally, RRKM assumes that, if the molecules are initially prepared with a nonrandom energy distribution, rapid intramolecular vibrational energy redistribution (IVR) will render the distribution a random one on a timescale much shorter than the molecules' unimolecular lifetime.[81] However, it is not unlikely that CID may produce short time non-statistical fragmentation. For example, Hase and co-workers recently reported different dissociation pathways and probabilities following thermal random excitation (*i.e.* after complete IVR) *vs.* short-time, non-random collisional activation of doubly protonated threonine-isoleucine-lysine.[82]

Rather than speculating, we defer the further discussion of these dynamics until we complete a direct dynamics trajectory study of [9HG·C–H]⁻. Three batches of trajectories are being propagated currently that either originate from activated 9HG·[C–H1]⁻ or 9HG·[C–H1]⁻_PT1, or start at the proton-transfer TS and move toward 9HG·[C–H1]⁻ or 9HG·[C–H1]⁻_PT1. Direct dynamic trajectories follow the motion of molecules, allowing the molecules to show us what the preferred pathways are; and the anharmonicity arising from multiple conformers and anharmonic vibrations is included in dynamics simulation. The simulation will be used to trace out non-RRKM kinetics from several perspectives: (1) identify the intrinsic reaction path at high energy where the molecule does not necessarily follow the minimum energy path, (2) identify the critical configurations in base pair dissociation so that we may improve the accuracy of unimolecular kinetic analysis, and (3) probe TS re-crossing by following the trajectories from the activation barrier for intra-pair proton transfer.

4 Conclusion

The present work used a combination of guided-ion beam tandem mass spectrometry and electronic structure theory (including B3LYP, M06-2X, PWPB95, RI-MP2 and DLPNO-CCSD(T) methods and a range of basis sets) to study the structures and dissociation of deprotonated G·C and 9MG·C base pairs. The CID mass spectrometric experiment has directly probed the two most stable structures for each deprotonated base pair: a conventional structure that is formed by the deprotonation of the cytosine N1–H site in neutral Watson–Crick base pairs and thus denoted as G·[C–H1]⁻ and 9MG·[C–H1]⁻, and a proton-transferred structure that is formed by intra-base-pair proton transfer within G·[C–H1]⁻ and 9MG·[C–H1]⁻ and thus denoted as G·[C–H1]⁻_PT1 and 9MG·[C–H1]⁻_PT1. The most striking finding is that there exists significant non-RRKM kinetics associated with proton transfer and/or dissociation of deprotonated G·C and 9MG·C. To obtain more insight into the origin of this non-statistical dynamics and kinetics, we are carrying out direct dynamics trajectory simulations, as alluded to above.

Acknowledgements

References

1 B. Boudaiffa, P. Cloutier, D. Hunting, M. A. Huels and L. Sanche, *Science*, 2000, **287**, 1658–1660.

2 S. Denifl, S. Ptasinska, M. Probst, J. Hrusak, P. Scheier and T. D. Maerk, *J. Phys. Chem. A*, 2004, **108**, 6562–6569.

3 R. R. Sinden, C. E. Pearson, V. N. Potaman and D. W. Ussery, *Adv. Genome Biol.*, 1998, **5A**, 1–141.

4 C. Sheu and C. S. Foote, *J. Am. Chem. Soc.*, 1993, **115**, 10446–10447.

5 Y. Ye, J. G. Muller, W. Luo, C. L. Mayne, A. J. Shallop, R. A. Jones and C. J. Burrows, *J. Am. Chem. Soc.*, 2003, **125**, 13926–13927.

6 W. L. Neeley and J. M. Essigmann, *Chem. Res. Toxicol.*, 2006, **19**, 491–505.

7 J. Cadet, T. Douki and J.-L. Ravanat, *Acc. Chem. Res.*, 2008, **41**, 1075–1083.

8 W. Lu and J. Liu, *Chem. – Eur. J.*, 2016, **22**, 3127–3138.

9 G. Palumbo, *Expert Opin. Drug Delivery*, 2007, **4**, 131–148.

10 W. Lu, H. Teng and J. Liu, *Phys. Chem. Chem. Phys.*, 2016, **18**, 15223–15234.

11 J. Bertran, A. Oliva, L. Rodriguez-Santiago and M. Sodupe, *J. Am. Chem. Soc.*, 1998, **120**, 8159–8167.

12 J. Florian and J. Leszczynski, *J. Am. Chem. Soc.*, 1996, **118**, 3010–3017.

13 L. Gorb, Y. Podolyan, P. Dziekonski, W. A. Sokalski and J. Leszczynski, *J. Am. Chem. Soc.*, 2004, **126**, 10119–10129.

This journal is © the Owner Societies 2016

Phys. Chem. Chem. Phys., 2016, **18**, 32222–32237 | 32235

14 M. Noguera, M. Sodupe and J. Bertrán, *Theor. Chem. Acc.*, 2004, **112**, 318–326.

15 M. Noguera, M. Sodupe and J. Bertrn, *Theor. Chem. Acc.*, 2007, **118**, 113–121.

16 J. D. Zhang, Z. Chen and H. F. Schaefer, III, *J. Phys. Chem. A*, 2008, **112**, 6217–6226.

17 H.-Y. Chen, C.-L. Kao and S. C. N. Hsu, *J. Am. Chem. Soc.*, 2009, **131**, 15930–15938.

18 H. Wang, J. D. Zhang and H. F. Schaefer, III, *ChemPhysChem*, 2010, **11**, 622–629.

19 Y. Lin, H. Wang, S. Gao and H. F. Schaefer, III, *J. Phys. Chem. B*, 2011, **115**, 11746–11756.

20 H.-Y. Chen, S.-W. Yeh, S. C. N. Hsu, C.-L. Kao and T.-Y. Dong, *Phys. Chem. Chem. Phys.*, 2011, **13**, 2674–2681.

21 Y. Lin, H. Wang, Y. Wu, S. Gao and H. F. Schaefer, III, *Phys. Chem. Chem. Phys.*, 2014, **16**, 6717–6725.

22 A. Szyperska, J. Rak, J. Leszczynski, X. Li, Y. J. Ko, H. Wang and K. H. Bowen, *ChemPhysChem*, 2010, **11**, 880–888.

23 Q. Gu and D. T. Haynie, *Annu. Rev. Nano Res.*, 2008, **2**, 217–285.

24 M. C. Lind, P. P. Bera, N. A. Richardson, S. E. Wheeler and H. F. Schaefer, III, *Proc. Natl. Acad. Sci. U. S. A.*, 2006, **103**, 7554–7559.

25 P. B. Armentrout, *Int. J. Mass Spectrom.*, 2000, **200**, 219–241.

26 U. Dornberger, M. Leijon and H. Fritzsche, *J. Biol. Chem.*, 1999, **274**, 6957–6962.

27 A. M. Ababneh, C. C. Large and S. Georghiou, *Biophys. J.*, 2003, **85**, 1111–1127.

28 Y. Fang and J. Liu, *J. Phys. Chem. A*, 2009, **113**, 11250–11261.

29 K. M. Ervin and P. B. Armentrout, *J. Chem. Phys.*, 1985, **83**, 166–189.

30 M. J. Frisch, G. W. Trucks, H. B. Schlegel, G. E. Scuseria, M. A. Robb, J. R. Cheeseman, G. Scalmani, V. Barone, B. Mennucci, G. A. Petersson, H. Nakatsuji, M. Caricato, X. Li, H. P. Hratchian, A. F. Izmaylov, J. Bloino, G. Zheng, J. L. Sonnenberg, M. Hada, M. Ehara, K. Toyota, R. Fukuda, J. Hasegawa, M. Ishida, T. Nakajima, Y. Honda, O. Kitao, H. Nakai, T. Vreven, J. J. A. Montgomery, J. E. Peralta, F. Ogliaro, M. Bearpark, J. J. Heyd, E. Brothers, K. N. Kudin, V. N. Staroverov, T. Keith, R. Kobayashi, J. Normand, K. Raghavachari, A. Rendell, J. C. Burant, S. S. Iyengar, J. Tomasi, M. Cossi, N. Rega, J. M. Millam, M. Klene, J. E. Knox, J. B. Cross, V. Bakken, C. Adamo, J. Jaramillo, R. Gomperts, R. E. Stratmann, O. Yazyev, A. J. Austin, R. Cammi, C. Pomelli, J. W. Ochterski, R. L. Martin, K. Morokuma, V. G. Zakrzewski, G. A. Voth, P. Salvador, J. J. Dannenberg, S. Dapprich, A. D. Daniels, O. Farkas, J. B. Foresman, J. V. Ortiz, J. Cioslowski and D. J. Fox, *Gaussian 09, Revision D.01*, Gaussian, Inc, Wallingford, CT, 2013.

31 O. O. Brovarets and D. M. Hovorun, *RSC Adv.*, 2015, **5**, 99594–99605.

32 J. Tomasi, B. Mennucci and R. Cammi, *Chem. Rev.*, 2005, **105**, 2999–3093.

33 Y. Zhao and D. G. Truhlar, *Acc. Chem. Res.*, 2008, **41**, 157–167.

34 L. Goerigk and S. Grimme, *J. Chem. Theory Comput.*, 2011, **7**, 291–309.

35 F. Weigend, M. Haser, H. Patzelt and R. Ahlrichs, *Chem. Phys. Lett.*, 1998, **294**, 143–152.

36 P. Jurecka, P. Nachtigall and P. Hobza, *Phys. Chem. Chem. Phys.*, 2001, **3**, 4578–4582.

37 D. G. Liakos, M. Sparta, M. K. Kesharwani, J. M. L. Martin and F. Neese, *J. Chem. Theory Comput.*, 2015, **11**, 1525–1539.

38 F. Neese, *Wiley Interdiscip. Rev.: Comput. Mol. Sci.*, 2012, **2**, 73–78.

39 I. M. Alecu, J. Zheng, Y. Zhao and D. G. Truhlar, *J. Chem. Theory Comput.*, 2010, **6**, 2872–2887.

40 S. Grimme, J. Antony, S. Ehrlich and H. Krieg, *J. Chem. Phys.*, 2010, **132**, 154104.

41 S. Grimme, S. Ehrlich and L. Goerigk, *J. Comput. Chem.*, 2011, **32**, 1456–1465.

42 R. A. Marcus, *J. Chem. Phys.*, 1952, **20**, 359–364.

43 L. Zhu and W. L. Hase, A General RRKM Program (QCPE 644), Quantum Chemistry Program Exchange, Chemistry Department, University of Indiana, Bloomington, 1993.

44 M. Liu, T. Li, F. S. Amegayibor, D. S. Cardoso, Y. Fu and J. K. Lee, *J. Org. Chem.*, 2008, **73**, 9283–9291.

45 S. A. Trygubenko, T. V. Bogdan, M. Rueda, M. Orozco, F. J. Luque, J. Sponer, P. Slavicek and P. Hobza, *Phys. Chem. Chem. Phys.*, 2002, **4**, 4192–4203.

46 E. Nir, M. Muller, L. I. Grace and M. de Vries, *Chem. Phys. Lett.*, 2002, **355**, 59–64.

47 E. Nir, C. Janzen, P. Imhof, K. Kleinermanns and M. de Vries, *Phys. Chem. Chem. Phys.*, 2002, **4**, 732–739.

48 R. D. Brown, P. D. Godfrey, D. McNaughton and A. P. Pierlot, *J. Am. Chem. Soc.*, 1989, **111**, 2308–2310.

49 B. F. Parsons, S. M. Sheehan, T. A. Yen, D. M. Neumark, N. Wehres and R. Weinkauf, *Phys. Chem. Chem. Phys.*, 2007, **9**, 3291–3297.

50 A. Zhachkina, M. Liu, X. Sun, F. S. Amegayibor and J. K. Lee, *J. Org. Chem.*, 2009, **74**, 7429–7440.

51 Y. Huang and H. Kenttamaa, *J. Phys. Chem. A*, 2004, **108**, 4485–4490.

52 A. K. Chandra, M. T. Nguyen, T. Uchimaru and T. Zeegers-Huyskens, *J. Phys. Chem. A*, 1999, **103**, 8853–8860.

53 E. C. M. Chen, C. Herder and E. S. Chen, *J. Mol. Struct.*, 2006, **798**, 126–133.

54 A. K. Chandra, M. T. Nguyen and T. Zeegers-Huyskens, *J. Mol. Struct.*, 2000, **519**, 1–11.

55 Y. Huang and H. Kenttaemaa, *J. Phys. Chem. A*, 2003, **107**, 4893–4897.

56 E. C. M. Chen, J. R. Wiley and E. S. Chen, *Nucleosides, Nucleotides Nucleic Acids*, 2008, **27**, 506–524.

57 Y. H. Jang, W. A. Goddard, III, K. T. Noyes, L. C. Sowers, S. Hwang and D. S. Chung, *J. Phys. Chem. B*, 2003, **107**, 344–357.

58 B. Song, J. Zhao, R. Griesser, C. Meiser, H. Sigel and B. Lippert, *Chem. – Eur. J.*, 1999, **5**, 2374–2387.

59 R. M. C. Dawson, D. C. Elliott, W. H. Elliott and K. M. Jones, *Data for Biochemical Research*, Clarendon Press, 1959.

60 Y. Seong, S. Y. Han, S.-C. Jo and H. B. Oh, *Mass Spectrom. Lett.*, 2011, **2**, 73–75.

61 R. D. Levine and R. B. Bernstein, *Molecular Reaction Dynamics and Chemical Reactivity*, Oxford University Press, New York, 1987.

62 J. Liu, B. Van Devener and S. L. Anderson, *J. Chem. Phys.*, 2002, **116**, 5530–5543.

63 P. de Sainte Claire, G. H. Peslherbe and W. L. Hase, *J. Phys. Chem.*, 1995, **99**, 8147–8161.

64 P. de Sainte Claire and W. L. Hase, *J. Phys. Chem.*, 1996, **100**, 8190–8196.

65 M. B. Sowa-Resat, P. A. Hintz and S. L. Anderson, *J. Phys. Chem.*, 1995, **99**, 10736–10741.

66 M. T. Rodgers, K. M. Ervin and P. B. Armentrout, *J. Chem. Phys.*, 1997, **106**, 4499–4508.

67 Y. Fang, A. Bennett and J. Liu, *Int. J. Mass Spectrom.*, 2010, **293**, 12–22.

68 C. Rebick and R. D. Levine, *J. Chem. Phys.*, 1973, **58**, 3942–3952.

69 W. J. Chesnavich and M. T. Bowers, *J. Phys. Chem.*, 1979, **83**, 900–905.

70 J. D. Zhang and H. F. Schaefer, III, *J. Chem. Theory Comput.*, 2007, **3**, 115–126.

71 P. Jurecka and P. Hobza, *J. Am. Chem. Soc.*, 2003, **125**, 15608–15613.

72 L. Zhu and W. L. Hase, *Chem. Phys. Lett.*, 1990, **175**, 117–124.

73 X. Hu, W. L. Hase and T. Pirraglia, *J. Comput. Chem.*, 1991, **12**, 1014–1024.

74 W. L. Hase, K. Bolton, P. de Sainte Claire, R. J. Duchovic, X. Hu, A. Komornicki, G. Li, K. Lim, D. Lu, G. H. Peslherbe, K. Song, K. N. Swamy, S. R. Vande Linde, A. Varandas, H. Wang and R. J. Wolf, *VENUS 99: A general chemical dynamics computer program*, Texas Tech Univeristy Lubbock, TX, 1999.

75 V. Bakken, J. M. Millam and H. B. Schlegel, *J. Chem. Phys.*, 1999, **111**, 8773–8777.

76 S. J. Klippenstein, A. L. L. East and W. D. Allen, *J. Chem. Phys.*, 1994, **101**, 9198–9201.

77 F. Meyer, F. A. Khan and P. B. Armentrout, *J. Am. Chem. Soc.*, 1995, **117**, 9740–9748.

78 M. B. More, E. D. Glendening, D. Ray, D. Feller and P. B. Armentrout, *J. Phys. Chem.*, 1996, **100**, 1605–1614.

79 D. Ray, D. Feller, M. B. More, E. D. Glendening and P. B. Armentrout, *J. Phys. Chem.*, 1996, **100**, 16116–16125.

80 W. L. Hase, *Acc. Chem. Res.*, 1983, **16**, 258–264.

81 D. L. Bunker and W. L. Hase, *J. Chem. Phys.*, 1973, **59**, 4621–4632.

82 Z. Homayoon, S. Pratihar, E. Dratz, R. Snider, R. Spezia, G. L. Barnes, V. Macaluso, A. Martin Somer and W. L. Hase, *J. Phys. Chem. A*, 2016, **120**, 8211–8227.

This journal is © the Owner Societies 2016

Phys. Chem. Chem. Phys., 2016, **18**, 32222–32237 | **32237**